SAND2010-5077P

Chapter 10
The Linear-Eddy Model

Suresh Menon and Alan R. Kerstein

Abstract Regime-independent modeling is important for accurate simulation of the complex combustor designs needed to meet increasingly stringent performance requirements. One strategy for achieving robust yet affordable predictive capability is to resolve, in space and time, the relevant advection-diffusion-reaction couplings using a low-dimensional representation of turbulent advection. In the linear-eddy model (LEM), this is accomplished in one spatial dimension by introducing an instantaneous map, the ’triplet map,’ that emulates the effect of an eddy turnover on property profiles along a notional line of sight. The map preserves the continuity of these profiles and obeys applicable conservation laws. Details and representative applications of the model are presented for passive and reactive scalar mixing, with emphasis on its use as a mixing-reaction closure for large-eddy simulation (LES) based on the embedding of an LEM domain in each LES control volume.

10.1 Motivation

Regime-independent modeling is a widely recognized goal of turbulent combustion modeling. This goal is driven by the need to model configurations involving various combinations of regimes such as partial premixing, extinction, re-ignition, recirculation, stratified premixed combustion, compression ignition, multi-stage ignition, and transition to detonation. Techniques involving coarse-graining, ensemble averaging, or state-space modeling face difficulties in this regard due to the lack of detailed representation of regime-specific advective-diffusive-reactive couplings.

S. Menon
School of Aerospace Engineering, Georgia Institute of Technology, USA, e-mail: `suresh.menon@aerospace.gatech.edu`

A. R. Kerstein
Combustion Research Facility, Sandia National Laboratories, Livermore, CA, USA, e-mail: `arkerst@sandia.gov`

Although progress in addressing these difficulties can be anticipated, the challenge of regime-independent modeling suggests the concurrent pursuit of an alternative approach, namely, the development of a conceptually and computationally minimal model that resolves, in space and time, some plausible representation of the coupled advancement of advection, diffusion, and reaction in turbulent reacting flow. The potential advantages of this strategy motivated the formulation, two decades ago, of the linear-eddy model (LEM) [29].

A useful starting point for introducing LEM is the numerical advancement of equations governing a 1D unsteady opposed-flow flame. This formulation can capture some but not all of the salient features of turbulent combustion. One important feature that it does not capture is the effect of rotational folding of the flame by turbulent eddy motions. Successive folding and compressive motions can cause an initially monotonic profile of, say, mixture fraction to develop multiple extrema with stoichiometric points in between, each corresponding to a flame location. At high turbulence intensity, the time scale of folding, compression, and diffusive mixing might become short enough relative to chemical time scales so that broad reaction zones, stirred internally by small eddies, are formed.

The impossibility of representing these effects in 1D by continuous-in-time motions while obeying the applicable conservation laws motivated the introduction, in LEM, of instantaneous maps. Each map can be conceptualized as representing the outcome of an individual eddy motion, although such a literal connection between maps and eddies is not required.

An LEM simulation time advances the 1D unsteady diffusion-reaction equations, including associated dilatations along the 1D domain. This advancement is punctuated by instantaneous rearrangements of property profiles by mapping operations of a specified form (see Sec. 10.2). In effect, the outcome of each map constitutes a new initial condition for further time advancement.

A numerical consequence of this procedure is that a time of map occurrence cannot be contained within a time step for advancement of the governing equations. This limits the potential advantage of implicit diffusion, so in LEM, diffusion is typically implemented explicitly, possibly with implicit chemistry depending on the stiffness of the kinetics.

Implementation of LEM as a subgrid model for large-eddy simulation (LES) has also been accomplished with the goal of applying it to more complex high Reynolds number flows. In this approach the LEM is coupled with a large-scale scalar transport method to capture both large-scale flame structures and subgrid wrinkling effects.

10.2 Triplet Map

It is convenient to define a map symbolically using the notation

$$s(y) \rightarrow s(M(y)), \tag{10.1}$$

where $s(y)$ is any property profile, y is the 1D spatial coordinate, and M is the inverse of the map, i.e., the property value at $M(y)$ is mapped to location y. The map used in LEM, termed the triplet map, has the form

$$M(y) = y_0 + \begin{cases} 3(y-y_0) & \text{if } y_0 \leq y \leq y_0 + \frac{1}{3}l, \\ 2l - 3(y-y_0) & \text{if } y_0 + \frac{1}{3}l \leq y \leq y_0 + \frac{2}{3}l, \\ 3(y-y_0) - 2l & \text{if } y_0 + \frac{2}{3}l \leq y \leq y_0 + l, \\ y - y_0 & \text{otherwise.} \end{cases} \tag{10.2}$$

This map shrinks property profiles within an interval $[y_0, y_0 + l]$ to a third of their original extent, and then fills the interval with three compressed copies of the profiles. The middle copy is reversed, which maintains the continuity of mapped properties and introduces the rotational folding effect of turbulent eddy motion (see Sec. 10.1). Property fields outside the size-l interval are unaffected.

On an unstructured adaptive 1D mesh, this spatial continuum definition of the triplet map can be implemented numerically as stated, as in an ODT adaptive-mesh implementation described in Chapter 11. Published LEM studies to date use a fixed uniform mesh, on which the triplet map is approximated as a permutation of mesh cells. It is convenient to focus on this implementation because its consistency with property conservation laws is self-evident.

Spatially discrete implementation of the triplet map is illustrated in Fig. 10.1, involving a permutation of cell indices j through $j+l-1$. Taking the map range l to be a multiple of 3 cells, the triplet map permutes the cell indices into the new order $j,\ j+3,\ j+6,\ \ldots,\ j+l-3,\ j+l-2,\ j+l-5,\ j+l-8,\ \ldots,\ j+4,\ j+1,\ j+2,\ j+5,\ j+8,\ \ldots,\ j+l-4,\ j+l-1$. This operation reduces the separation of any pair of cells by no more than a factor of three, consistent with the scale locality of length-scale reduction by eddy motions in the turbulent cascade (see Chapter 11).

It is interesting to note that the triplet map and its uses for turbulence simulation were discussed in a recent paper by authors who developed this concept without knowledge of prior work on LEM [28]. This is perhaps indicative of the degree to which map-based advection using the triplet map is a uniquely advantageous approach for economical turbulent-mixing simulation.

10.3 Map Sizes and Frequency of Occurrence

As explained in Sec. 10.1, LEM is intended to be an alternative to models involving coarse-grained constructs such as eddy diffusivity D_T. Although eddy diffusivity is not the modality of turbulent transport implementation in LEM, it is central to LEM formulation. Eddy diffusivity parameterizes the aggregate turbulent transport induced by an ensemble of turbulent eddies. Accordingly, the ensemble of triplet maps during an LEM simulation induce aggregate transport that is quantifiable as an eddy diffusivity, here denoted D_T. Based on the triplet-map property that it induces a mean-square displacement $\frac{4}{27}l^2$ within the mapped interval, random-walk theory

$$\begin{matrix} \mathbf{1}&0&0&0&0&0&0&0&0&0&0&0&0&0&0&0 \\ 0&\mathbf{1}&0&0&0&0&0&0&0&0&0&0&0&0&0&0 \\ 0&0&\mathbf{1}&0&0&0&0&0&0&0&0&0&0&0&0&0 \\ 0&0&0&\mathbf{1}&0&0&0&0&0&0&0&0&0&0&0&0 \\ 0&0&0&0&0&0&\mathbf{1}&0&0&0&0&0&0&0&0&0 \\ 0&0&0&0&0&0&0&0&0&\mathbf{1}&0&0&0&0&0&0 \\ 0&0&0&0&0&0&0&0&0&0&\mathbf{1}&0&0&0&0&0 \\ 0&0&0&0&0&0&0&\mathbf{1}&0&0&0&0&0&0&0&0 \\ 0&0&0&0&\mathbf{1}&0&0&0&0&0&0&0&0&0&0&0 \\ 0&0&0&0&0&\mathbf{1}&0&0&0&0&0&0&0&0&0&0 \\ 0&0&0&0&0&0&0&0&\mathbf{1}&0&0&0&0&0&0&0 \\ 0&0&0&0&0&0&0&0&0&0&0&\mathbf{1}&0&0&0&0 \\ 0&0&0&0&0&0&0&0&0&0&0&0&\mathbf{1}&0&0&0 \\ 0&0&0&0&0&0&0&0&0&0&0&0&0&\mathbf{1}&0&0 \\ 0&0&0&0&0&0&0&0&0&0&0&0&0&0&\mathbf{1}&0 \\ 0&0&0&0&0&0&0&0&0&0&0&0&0&0&0&\mathbf{1} \end{matrix} \quad \begin{matrix} 16 \\ 15 \\ 14 \\ 13 \\ 12 \\ 11 \\ 10 \\ 9 \\ 8 \\ 7 \\ 6 \\ 5 \\ 4 \\ 3 \\ 2 \\ 1 \end{matrix} \quad = \quad \begin{matrix} 16 \\ 15 \\ 14 \\ 13 \\ 10 \\ 7 \\ 6 \\ 9 \\ 12 \\ 11 \\ 8 \\ 5 \\ 4 \\ 3 \\ 2 \\ 1 \end{matrix}$$

Fig. 10.1: Application of a triplet map with $l = 9$, formulated as a permutation matrix multiplying a vector representing a flow state. Here, the map is applied to a column vector with vertically increasing cell indices. For clarity, unity matrix elements are boldface and cells are shifted horizontally in proportion to their index values. The shifts are intended to suggest the 1D profile of a mapped variable.

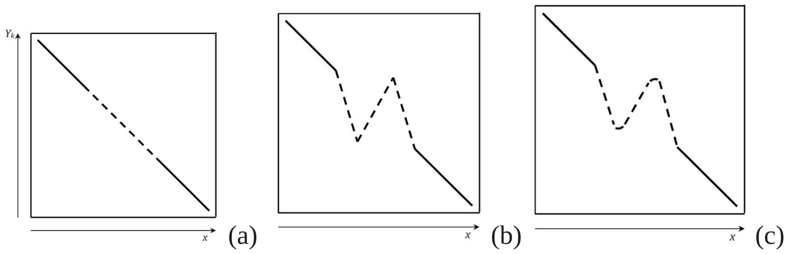

Fig. 10.2: Scalar field evolution with LEM. (a) initial field, (b) after triplet map and (c) after diffusion-reaction equation

allows D_T to be expressed as

$$D_T = \frac{2}{27} \Lambda \int_0^\infty l^3 f(l)\, dl, \tag{10.3}$$

where $f(l)$ is the probability density function (PDF) of map sizes (a model input) and Λ is the frequency of map occurrences per unit domain length, so that Λ times the domain size is the rate of map occurrence on a notional spatially homogeneous domain [33]. (In previous model descriptions, the notation λ rather that Λ was used in Eq. 10.3. Here, the notation is changed for consistency with Chapter 11.) Equation 10.3 is used to solve for Λ given a D_T value and a size distribution $f(l)$ that correspond to the turbulent flow that is being simulated.

The functional form of $f(l)$ is based on the following familiar consequence of internal-range turbulence scaling. The eddy diffusivity $D_T(l)$ associated with turbulent motions of size l or less scales as $lv(l)$, where the eddy velocity $v(l)$ scales as $l^{1/3}$, so $D_T(l) \sim l^{4/3}$. The LEM analog of $D_T(l)$ is obtained by taking l to be the upper bound of the integral in Eq. 10.3 (to be distinguished from the dummy variable l in the integrand). The map-size PDF that yields this scaling is $f(l) \sim l^{-8/3}$.

The inertial range extends from the Kolmogorov microscale η to the integral scale L, which obey the scaling $L/\eta \sim \mathrm{Re}^{3/4}$, where Re is the integral-scale Reynolds number, $Re = u'L/\nu$, and u' is the turbulence intensity. Therefore, the stated scaling of f extends from η to L, and $f = 0$ outside this range. This determines the prefactor of f by the requirement that its integral over l is unity.

Here, η and L do not have precisely the same meanings in LEM as in turbulent flow, so strictly speaking these LEM quantities are related to their physical counterparts by empirical coefficients. Likewise, turbulent diffusivity values inferred from flow data typically do not precisely conform to the mathematical definition of a diffusivity, so an empirical coefficient may be needed to relate these values to the LEM parameter D_T, which has a precise definition within the model.

10.4 Application to Passive Mixing

For passive mixing involving a single scalar property s with constant molecular diffusivity κ, time advancement between map occurrences is governed by the heat equation,

$$\frac{\partial s}{\partial t} = \kappa \frac{\partial^2 s}{\partial y^2} \tag{10.4}$$

The equation set for combustion is shown in Sec. 10.5.

For passive mixing, the family of scalar power spectra parameterized by the Schmidt number Sc is a useful comparison data set for LEM because the spectra exhibit universal behaviors with a sufficient number of features to overdetermine the model and test its performance. Spectrum comparisons have been used to set the free parameters in LEM and to demonstrate that LEM captures the salient features of turbulent mixing [6, 33]. Figure 10.2 shows a typical implementation and competition between molecular diffusion and turbulent stirring by the triplet mapping. Turbulent stirring on an initial scalar gradient mimics the folding effect of an eddy of size l with the subsequent molecular diffusion smoothing the gradient. These processes interact over a range of eddy sizes in a high Re flow resulting in statistical features of scalar mixing in excellent agreement with classical scaling laws and experimental observations.

For example, LEM as described above has been applied to mixing in grid turbulence (including three-stream mixing) [29, 34], in planar mixing layers (focusing on Sc dependence) [30], and in multi-scalar jet and homogeneous flows that exhibit differential molecular diffusion effects [6, 31, 36]. An application to mixing in homogeneous turbulence [38] revealed unexpected large-scale mixing behaviors that were subsequently verified by a pipe-flow experiment motivated by the LEM results [22–24]. Other homogeneous-turbulence studies compared scalar fluctuation decay in LEM and direct numerical simulations (DNS) [7, 44] and used LEM to study fractal scaling properties [32] and other intermittency properties [27, 33] of scalar fields mixed by turbulence.

The mixing of dry and moist air in clouds has been simulated using LEM in order to study temperature changes induced by cloud droplet evaporation and condensation and associated dynamical consequences [42, 43]. These studies, which were extended to simulate the evolution of droplet-size distributions [76], did not incorporate buoyancy effects but provided indications of larger-scale consequences of buoyancy changes during the simulations. It has been shown mathematically that triplet maps, in conjunction with a simple represention of eddy-induced motion of inertial particles, capture clustering effects thought to be crucial to the process of cloud-droplet coagulation to form raindrops [37].

10.5 Application to Reacting Flows

For reacting flows, the LEM employs more general equations for the species and temperature within the 1D context. An extension of the LEM to multi-component reacting flows can be written as [53, 54, 72, 75, 79] :

$$
\begin{aligned}
\rho \frac{\partial Y_k}{\partial t} &= -\frac{\partial}{\partial y}(\rho Y_k V_k) + \dot{\omega}_k \\
\rho C_{p_{mix}} \frac{\partial T}{\partial t} &= -\rho \frac{\partial T}{\partial y}\left(\sum_{k=1}^{Ns} C_{p,k} Y_k V_k\right) + \frac{\partial}{\partial y}\left(\kappa \frac{\partial T}{\partial y}\right) + \dot{\omega}_T
\end{aligned}
\tag{10.5}
$$

Here, Y_k is the $k-$th species mass fraction, $\dot{\omega}_k$ is the reaction rate, and V_k is the $k-$th species diffusion velocity.

Any type of kinetics (global or multi-step) can be included within this approach. Heat release related effects such as thermal expansion and mass transport to maintain global conservation have to be included but their specific implementation issues depend on the problem of interest [1, 48, 72, 79]. An example of the advantages of LEM reactive-flow simulation relative to other approaches is an application [14] to two simple reaction mechanisms that are widely used as test cases for closure models. LEM was shown to be in agreement with DNS of these reactions in a non-premixed configuration. LEM was then used to investigate a much wider parameter range than DNS can access affordability, yielding a data set suitable for stringent tests of proposed closures. None of the tested closures reproduced LEM product-selectivity results.

LEM has likewise been used to evaluate proposed nonpremixed-combustion closures [8, 9]. *A priori* analysis of the LEM-predicted PDF of the scalar properties has been shown to agree very well with experimental PDFs for jet diffusion flames [20]. It has also been used to explore regimes that closure models cannot yet address adequately, such as soot-radiation-turbulence coupling [80], and in applied studies such as NOx prediction in dual-stage combustion [52], jet flames [1, 48], aerosol mixing in engine exhaust [53, 79], and transient behaviors during incineration [66].

More recent studies include the study of extinction/re-ignition for a non-premixed syngas flame [68–71] for a test case simulated earlier by DNS [25, 26] using the same 21-step, 11-species skeletal syngas mechanism. Results showed the LEM can capture both the extinction and re-ignition process at approximately the same turbulent Reynolds number with the scalar dissipation rate at the stoichiometric surface predicted to be 2394 1/s, which is very close to the DNS value of 2100 1/s.

Many canonical premixed flames have also been investigated using the LEM. Freely propagating turbulent premixed flames in the flamelet regime [49, 72, 73] and in the thin-reaction-zone regime [61] have demonstrated that the changes in the flame structure can be captured without any change to the LEM. Recent stand-alone premixed LEM studies have focused on premixed combustion far from the flamelet regime. LEM has been applied to regimes of hydrogen [56] and hydrocarbon combustion relevant to homogeneous-charge compression-ignition (HCCI) combustion. An application to astrophysical flames [78] validated LEM using DNS of the well-stirred-reactor regime, then explored the more challenging ‘stirred-flame’ regime [35] to identify possible mechanisms for transition to detonation resulting in supernova explosions. Additionally, this study showed that the LEM turbulent burning velocity in the flamelet regime is $18D_T/L$ for high Re, a result that is useful for detecting departures from flamelet or high-Re scaling.

Recent studies employed the LEM to investigate flame-turbulence interactions for a range of conditions and fuel mixture with relatively detailed reduced kinetics [70, 71]. We use some results from this study to highlight key features of the LEM when implemented for reacting flows. For this study, the LEM scalar fields are initialized by the steady, laminar, 1D flame solution obtained for a CH_4/Air mixture at an equivalence ratio of 0.6, and a 12-step, 16-species reduced methane/air mechanism is used for the calculations. Thermally perfect gas with detailed multi-component transport properties is employed for these simulations.

Figure 10.3 compares a typical H_2 mass fraction profile that has evolved from the initial laminar profile with stirring alone (Fig. 10.3, top left), with profiles evolved by stirring and diffusion (Fig. 10.3, top right) together, and with stirring, diffusion and reactions interacting (Fig. 10.3, bottom), which is the full LEM. It can be seen that the profile is wrinkled and exhibits high level of scalar gradients as a result of the turbulent stirring (Fig. 10.3, top left) but once the diffusion is included the gradients created by the triplet-maps are smoothed out (Fig. 10.3, top right). The peak value for the H_2 intermediate species decreases as well, which indicates that the flame is extinguishing, since reaction rates are not computed and the combined action of the turbulent stirring and diffusion pushes the flame towards extinction. However, when kinetics is also included (Fig. 10.3, bottom) the flame maintains its peak value while

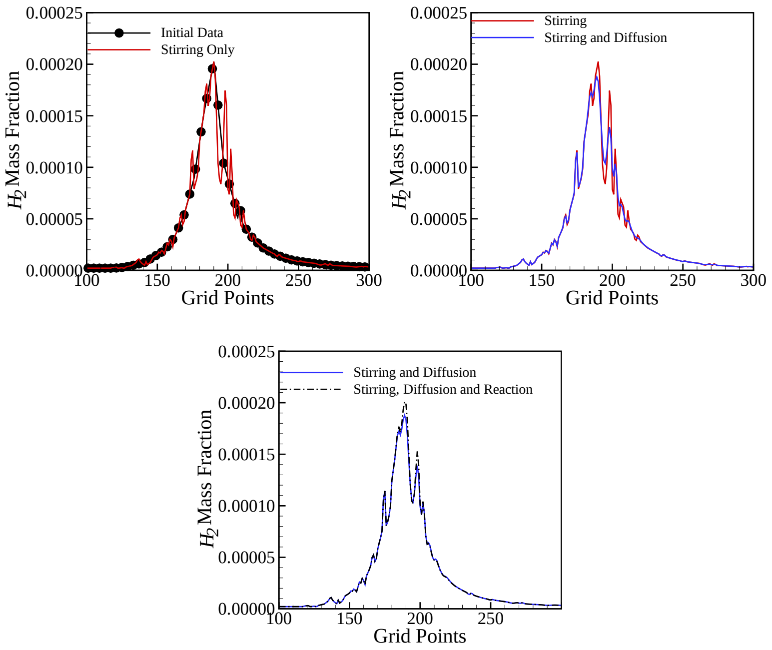

Fig. 10.3: Evolution of a scalar field (H_2) by simulating the effect of stirring (top left), stirring and diffusion (top right), and stirring, diffusion and reaction (bottom).

also showing the effect of stirring and diffusion. Thus, turbulent stirring, molecular diffusion and reaction kinetics can interact at their respective time scales in the LEM in a consistent manner. This is the unique nature of the LEM.

10.6 Application to Reacting Flows as a Subgrid Model

Extension of the LEM as a subgrid model requires some rethinking of the turbulent stirring approach described above. In the classical LES methodology large scale structures are fully resolved whereas small scale structures (sub-grid-scale) are modeled by using appropriate sub-grid momentum and combustion models. Thus, closures for momentum, energy and scalar transport at the resolved scales are required. This requirement is no different from the closure requirement for RANS modeling, and an earlier effort [18, 19] demonstrated a LEM based approach for RANS application. In the following, we focus primarily on the LES implementation of LEM (called LEMLES hereafter).

For LES of reacting flows, both low-Mach number [2, 3] and fully compressible approach have been used in the past. Closure for the momentum and energy equation is achieved using a localized dynamic subgrid kinetic energy k^{sgs} model (LDKM) [17, 39–41, 50, 54, 55] in most of the studies discussed here. In addition to allowing for non-equilibrium between production and dissipation at the subgrid scales, the LDKM offers two unique advantages for LEMLES that is absent in the classical Smagorinsky type algebraic eddy viscosity mode: (a) the k^{sgs} distribution can be used to provide an estimate of the subgrid turbulence intensity $u' \approx \sqrt{2k^{sgs}/3}$, which can then be used for estimating turbulent stirring time scale and frequency in the subgrid LEM, and (b) for two-phase modeling of spray combustion, a stochastic component to the particle motion can be included to account for the effect of subgrid turbulence on particle transport [46, 54, 58] The governing LES equations for mass, momentum and energy are obtained by using density-weighted Favre-filtering and the following discussion, although restricted to compressible flows is equally applicable in low-Mach number flows [3, 5].

The LEM-based subgrid closure for mixing and chemistry was developed [45, 51] for both premixed and non-premixed applications, and has been used for LES closure in many subsequent studies, e.g., scalar mixing [6, 47], non-premixed combustion [11, 47, 68, 70], premixed combustion [3, 5, 61, 63, 74, 77], two-phase combustion [54, 57, 58], soot formation [12, 13] and supersonic mixing and combustion [62]. This closure introduces an LEM domain in each control volume of the 3D mesh. The LEM domain size is of the order of the resolution scale of the 3D mesh, and evolves a 1D profile of the thermochemical state that serves as a representative sample of evolution within the control volume that contains it. Specializing to LES closure, the LES time-advancement cycle begins with an update of the coarse-grained LES flow state, consisting of velocity components and density. (All thermochemical information resides solely within the LEM domains.) Next, diffusive transport, chemistry, and triplet maps representing subgrid advection are implemented within each subgrid LEM domain for a time interval equal to the LES time step. Then the LEM domains communicate with each other by means of a ‘splicing’ procedure (see Fig. 10.6). The mass transfer across each LES mesh face during the LES time step is computed based on the LES-resolved velocity and density. The prescribed transfer is applied to the affected LEM domains by excising a piece of the domain that is upwind of the LES face and inserting it into the LEM domain that is downwind of the LES face. These processes are schematically shown in Fig. 10.4 and indicate that the LEM subgrid model can be implemented within any flow solver without any major revision to the original structure of the fluid dynamics solver.

To describe this model mathematically, we split the velocity field as: $u_i = \tilde{u}_i + (u_i')^R + (u_i')^S$. Here, $\tilde{u}_i$ is the LES-resolved velocity field, $(u_i')^R$ is the LES-resolved subgrid fluctuation (obtained from k^{sgs}) and $(u_i')^S$ is the unresolved subgrid fluctuation. Then, consider the *exact* species equation (i.e., without any explicit LES filtering) for the k-th scalar Y_k written in a slightly different form as:

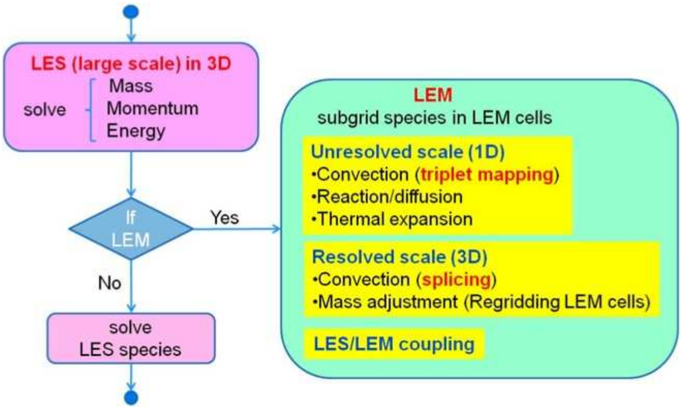

Fig. 10.4: Schematic of the LEMLES approach

$$\rho\frac{\partial Y_k}{\partial t} = -\rho[\tilde{u}_i + (u_i')^R + (u_i')^S]\frac{\partial Y_k}{\partial x_i} - \frac{\partial}{\partial x_i}(\rho Y_k V_{i,k}) + \dot{w}_k + \dot{S}_{s,k} \qquad (10.6)$$

Here, $V_{i,k}$ are the $k-th$ species diffusion velocity and $\dot{S}_{s,k}$ is a source term if there is phase change as in vaporization of liquid fuel. In LEMLES, the above equation is rewritten in a two-step process as:

$$Y_k{}^* - Y_k{}^n = \int_t^{t+\Delta t_{LES}} -\frac{1}{\rho}[\rho(u_i')^S\frac{\partial Y_k{}^n}{\partial x_i} + \frac{\partial}{\partial x_i}(\rho Y_k V_{i,k})^n - \dot{w}_k^n - \dot{S}_{s,k}^n]dt' \qquad (10.7)$$

$$\frac{Y_k{}^{n+1} - Y_k{}^*}{\Delta t_{LES}} = -[\tilde{u}_i + (u_i')^R]\frac{\partial Y_k{}^n}{\partial x_i} \qquad (10.8)$$

Here, Δt_{LES} is the LES time-step. Equation 10.7 describes the subgrid LEM model, as viewed at the LES space and time scales. The integrand includes four processes that occur within each LES grid cell, and represent, respectively, (i) subgrid molecular diffusion, (ii) reaction kinetics, (iii) subgrid stirring, and (iv) phase change of the liquid fuel. These processes are modeled on a 1D domain embedded inside each LES grid where the integrand is rewritten in terms of the subgrid time and space scales. Equation 10.8 describes the large-scale 3D LES-resolved convection of the scalar field, and is implemented by a Lagrangian transfer of mass across the finite-volume cell surfaces [3, 47]. Descriptions for the subgrid processes (in Eq. 10.7) and the 3D advection process (in Eq. 10.8) are presented elsewhere [54] but are repeated here for completeness.

As shown in Eqs. 10.7 and 10.8, and in Fig. 10.4, there are two different elements to the LEMLES. We will consider the subgrid LEM (the integrand in Eq. 10.7) and the resolved-scale transport (Eq. 10.8) separately.

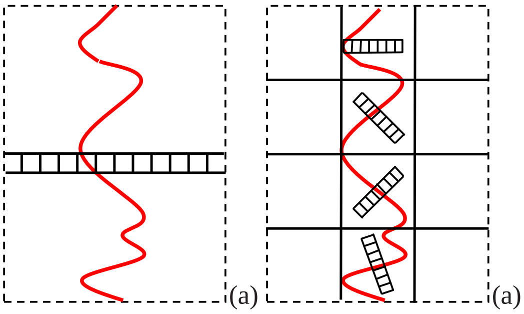

Fig. 10.5: Schematic representation of the LEM domain and the flame for (a) stand-alone LEM, (b) LEMLES.

10.6.1 The LEM Subgrid Model

The LEM is implemented within the LES cells as a subgrid model and Eqs. 10.5 are solved within each LES cell. In stand-alone LEM simulations the one-dimensional domain extends across the flame, whereas in the LEMLES approach they are embedded within each LES cell. This is schematically shown in Figs. 10.5a-b. The LEM domains are independent from each other and the 1D line is notionally aligned in the flame normal or the maximum scalar gradient direction and thus, does not represent any physical Cartesian direction.

Since all the turbulent scales below the grid are resolved in this approach, both molecular diffusion and chemical kinetics are closed in an exact manner. As a result, scalar “subgrid” terms do not have to be closed or modeled. The sub-grid pressure, p^{LEM} is assumed constant over the LEM domain, and equal to the LES value, $\overline{p}$, which is a valid assumption in the absence of strong pressure gradients. Hence, the sub-grid density is computed from the equation of state at the sub-grid level :

$$p^{LEM} = \rho^{LEM} T^{LEM} \sum_{k=1}^{N_{species}} Y_k^{LEM} \frac{R_u}{W_k} \tag{10.9}$$

Here, W_k is the $k-th$ species molecular weight.

Conservation of mass, momentum and energy (at the LES level) and conservation of mass, energy and species (at the LEM level) are fully coupled. Chemical reaction at the LEM level determines heat release and thermal expansion at the LEM level, which at the LES level generates flow motion that, in turn, transports the species field at the LEM level. Full coupling is maintained in the LEMLES to ensure local mass conservation.

The reaction-diffusion equation on the LEM domain is solved within each LES with an explicit scheme. The time integration is achieved by using an operator splitting technique to account for four distinct physical processes and time scales in the LEM (molecular diffusion, chemistry, turbulent stirring and thermal expansion). The diffusion time step is calculated as: $\Delta t_{diff} = C_{diff} \frac{\Delta s^2}{\max(D_k)}$. The maximum of D_k is used for Δt_{diff} in order to maintain the stability of the diffusion of the lightest species. The C_{diff} in the equation is a model constant, set here to 0.25 for numerical stability [64]. The chemical time step size is determined by the stiffness of the reaction mechanism. The stiffness increases as the number of radical species in a chemical kinetics mechanism increases. The chemistry is integrated for the given diffusion time step size (Δt_{diff}). A stiff ODE solver which uses adaptive time step size is employed for the integration process so that the chemical processes are resolved in their respective time scales. This approach, nevertheless, is very time consuming, and therefore, novel methods such as in-situ adaptive tabulation [12, 13] and artificial neural network [68, 70, 71] have been implemented within LEM to achieve speed-up.

The thermal expansion time scale is associated with the volumetric expansion induced by the increase in temperature through chemical heat release. In the current implementation $\Delta t_{expansion} \approx \Delta t_{diff}$, and turbulent stirring is implemented as discrete time events during the reaction-diffusion time integration. The time interval between each stirring event is: $\tau_{stir}(x) = 1/\Lambda\overline{\Delta}$, where Λ is the stirring frequency described earlier, and $\overline{\Delta}$ is the LES grid filter size. Overall, for the given LES time step, the number of stirrings events is equal to $N_{stir} \approx \Delta t_{LES}/\Delta t_{stir}$.

In different implementations of this closure strategy, LEM domains can have either periodic [51] or Neumann boundary conditions [54]. In the former method the spliced pieces can be excised and inserted at arbitrary locations or a type of first-in-first-out criterion can be applied. In the latter approach the LEM domain has an input side and an output side. A common characteristic of these implementations is that the LEM domains are Lagrangian objects that have no unique spatial location or orientation within the LES control volume that contains them.

10.6.2 Large-Scale Advection of the Subgrid Field

The large scale advection is implemented in LEMLES to account for the advection of the scalar field on the resolved level between the LES cells according to Eq. 10.8. This process accounts for species transport in the 3D domain due to both the resolved LES velocity field $\widetilde{u_i}$ and the resolved subgrid kinetic energy k^{sgs}. Since the scalar structure is inherent in the subgrid LEM cells, they are transported across the LES fields by a Lagrangian transport process. This is in contrast to a conventional finite-volume or finite-difference approximation of the filtered scalar gradients across LES cells. Thus, the right hand side of Eq. 10.8 is not discretized using a conventional difference operator but rather, the convection of the subgrid scalar field (and hence the subgrid scalar gradient, $\partial Y_k/\partial s$) is explicitly carried out by the Lagrangian splicing approach.

The advection process is implemented once the subgrid evolution of the scalar field as a result of the turbulent stirring, diffusion, reaction and thermal expansion

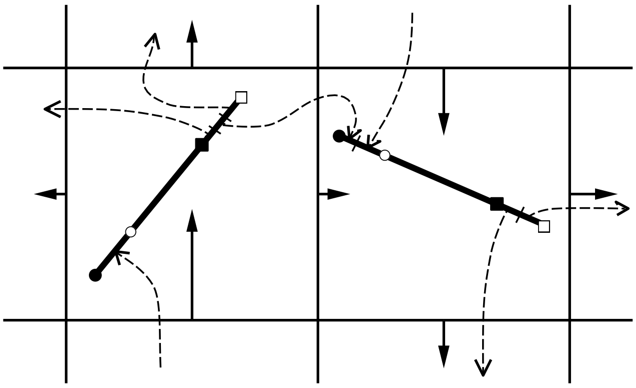

Fig. 10.6: Illustration of the splicing strategy, in which thermochemical information resides solely within LEM domains (tilted line segments) contained with control volumes of the 3D solver, but flow evolves on the coarse 3D mesh. Solid lines with arrows are flow velocities, evolved on the coarse mesh, that determine volume transfers between 1D subgrid domains. The splicing mechanism that implements these transfers is illustrated. Each LEM domain has an input end (circle) and an output end (square). Open and filled symbols demarcate the LEM domains before and after splicing. Portions transferred during splicing are separated by tick marks. Dashed curves with arrows indicate transfers between 1D domains in different control volumes. An alternative to specified input and output locations is to use periodic LEM domains. Then there are no preferred locations at which to remove and insert domain segments unless a first-in-first-out type of criterion is introduced.

are completed at their respective time steps. The large scale advection is a result of both the resolved large scale ($\tilde{u}_i$) and the modeled subgrid scale velocities ($({u'}_i)^R$). In the current implementation, based on the assumption that the velocity field is isotropic on the small scales, $({u'}_i)^R$ is estimated: $({u'}_i)^R = \sqrt{\frac{2}{3}k_{sgs}}$. However, if k_{sgs} is not available this additional flux cannot be included. Regardless, this contribution is very small and in most cases can be neglected.

Equation 10.8 can be written in a finite volume discrete form as follows,

$$\frac{(\rho Y_k)^{n+1}\Delta V-(\rho Y_k)^{*}\Delta V}{\Delta t_{LES}}=-\sum_{j=1}^{N_f}\rho_j\left(\tilde{u}_i+(u_i')^R\right)_j {Y_k}^{*}A_j \tag{10.10}$$

where ΔV is the volume of a finite volume cell, N_f is the number of cell face, and A_j is the cell face area. The large-scale advection of the sub-grid scalar *structure*, Y_k is based on the mass flux across each cell face. Therefore, Eq. 10.10 can be rewritten by defining $m = \rho\Delta V$ and rearranging,

$$(mY_k)^{n+1} = (mY_k)^* - \Delta t_{LES} \sum_{j=1}^{N_f} (\delta mY_k)_j \tag{10.11}$$

where $\delta m = \rho \left(\tilde{u_i} + (u_i')^R\right) A_j$, which is the mass flux that crosses a cell face, A_j. The last term in (10.11) is further decomposed into influx and outflux components. Therefore, Eq. 10.11 becomes,

$$(mY_k)^{n+1} = (mY_k)^* - \Delta t_{LES} \left[-\sum_{N_{in}} (\delta mY_k)_{in} + \sum_{N_{out}} (\delta mY_k)_{out} \right] \tag{10.12}$$

where N_{in} and N_{out} are the number of influx and outflux faces surrounding a finite volume cell. Here, $(\delta mY_k)_{in}$ is computed by taking portions of the mass contained in LEM cells in the neighboring finite volume cells. The mass in N_{splice} LEM cells is collected based on the net in-flux and added to the LEM cells in the current finite volume cell. At the same time, $(\delta mY_k)_{out}$ is computed from the mass contained in LEM cells in the current finite volume cell and distributed to the neighboring LES cells based on the out-flux. With proper care to advect the total mass based on convective flux, proper mass conservation can be strictly enforced during this process. Since this process is also in full 3D, the advection of the *subgrid* scalar gradients by this Lagrangian process allows transport of both co-gradient and counter-gradient subgrid structure across LES cell faces. This is a unique strength of this advection process when compared to conventional gradient diffusion modeled at the LES level by a standard finite-difference or finite-volume method.

Due to compressibility, volumetric expansion and grid-stretching, N_{splice} may be different than N_{LEM} (the number of LEM cells in each LES grid volume) and this is included in the formulation. Furthermore, N_{splice} need not be an integer and the current algorithm allows for fractions of individual subgrid volumes to be transported, whereas the predetermined N_{LEM} is an integer multiple of 3, and greater than 9 to accommodate the triplet mapping procedure.

Once all the mass is transferred between the LES cells, the new LEM field can have more or less cells than that it had before the splicing started, as shown in Fig. 10.7. Also, the volume of the cells can be different from each other based on the transferred mass. Re-gridding is applied to uniformly divide all the mass between LEM cells. This process is schematically shown in Fig. 10.8. Re-gridding is strictly not needed if a variable subgrid domain is employed and is done primarily for numerical expediency. As in any simplification resulting errors have to be considered. For example, if re-gridding changes the composition in the LEM cells then it is considered artificial diffusion. This artificial diffusion can be minimized by increasing the number of LEM cells or by splicing smaller amounts of mass. While the former is essentially a grid refinement strategy, the latter is constrained by the time-step of the flow solver and cannot be arbitrarily changed. In compressible explicit flow solvers, due to the small LES time-step, the numerical diffusion effect is indeed very small. Nevertheless, this artifact of the LEM implementation should be eliminated for overall accuracy, and therefore, a more general implementation of the LEM (with variable subgrid resolution) is being pursued.

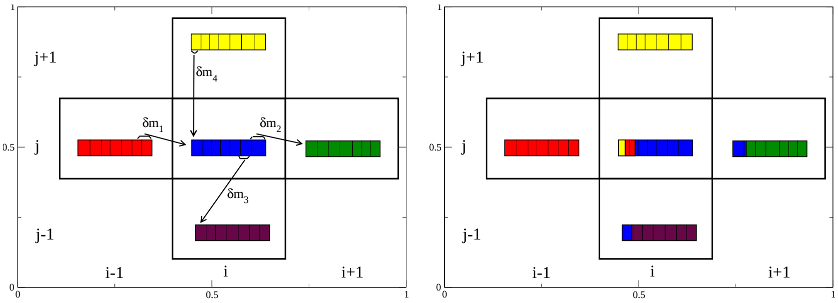

(a) Before splicing (b) After splicing

Fig. 10.7: Species field before and after the splicing of the cell (i, j).

The Lagrangian advection process can track interfaces accurately. For example, Fig. 10.9 shows advection of an annular box without loss of its integrity in a uniform flow oriented along the diagonal of the simulation domain. The mass-flux based transport process allows counter-gradient transport of scalars (since subgrid scalar structures are transported by splicing), enabling the model to avoid the pit-falls of those based on the gradient-diffusion hypothesis. Figure 10.10 shows the propagation of a circular burning flame, which includes both subgrid burning and thermal expansion effects. The circular flame is resolved on a Cartesian grid with reasonable accuracy [3].

Implementation of splicing is relatively straightforward and visually summarized in Fig. 10.7. Splicing is composed of the following steps: (1) calculate the LES flux, $\rho(\tilde{u}_i+(u'_i)^R)$ on each of the six faces of the volume, (2) determine the amount of mass to send as well as the amount of mass to receive from the neighboring LES cells, (3) arrange the LES fluxes with the largest out-flux carried out first in accordance with the premise that the 1D scalar fields are always aligned in the direction of the maximum scalar gradient, and (4) after the receipt of mass from each face commensurate with step 2, rearrange the scalar field in each cell accordingly. Re-gridding then follows, if there are heat release effects. As noted earlier, re-gridding is a numerical artifact intended for simplicity and can be eliminated with a more general formulation.

The ability of the Lagrangian advection to capture the flame structure is summarized in Fig. 10.11, which compares a 3D simulation of a turbulent premixed flame conducted using DNS and LEMDNS [63]. The latter approach implies that the LES grid is as fine as the DNS grid but the LEM was included within the subgrid. Thus, in the DNS limit the splicing process occurs only due to the resolved velocity field and the LEM subgrid processes are reduced to only diffusion and kinetics (i.e., stirring is turned off). The excellent agreement between a DNS and the LEMDNS shows

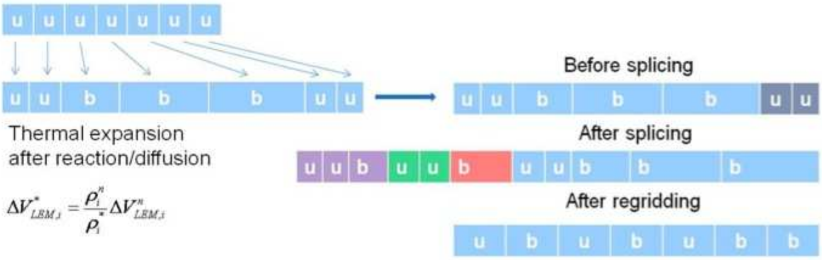

Fig. 10.8: Schematic representation of the subgrid scalar field after thermal expansion and re-gridding. Here *u* and *b* indicate an unburned and a burned LEM cell, respectively.

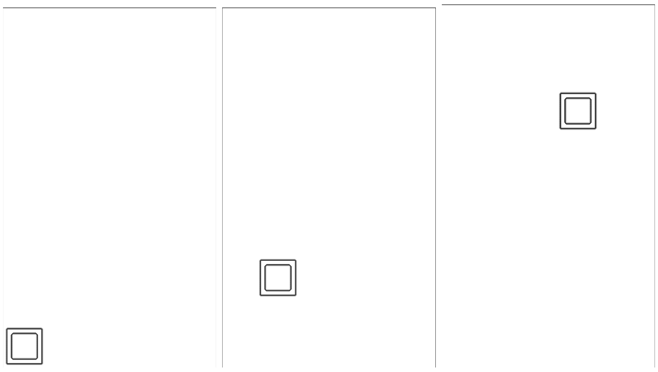

Fig. 10.9: Propagation of an annular box in a velocity field aligned along the diagonal.

that the physically consistent and correct implementation of the scalar evolution by the two-step procedure (Eqs. 10.7 and 10.8).

A recently developed alternative LEM-based subgrid closure called LEM3D [65] has a well-defined spatial structure. In fact, its structure is the same as in ODTLES [67], a method for 3D flow advancement involving an array of coupled 1D domains, using the one-dimensional turbulence (ODT) model (see Chapter 11).

An advantage of LEM3D relative to the splicing strategy is that it avoids the imposition of Neumann boundary conditions on LEM within each 3D control volume, which is the currently preferred splicing formulation. A related advantage is that a triplet map need not be contained within one 3D control volume, nor need it be limited in size relative to the control volume. An advantage of the splicing strategy is that it is readily implemented within an arbitrary structured or unstructured mesh. LEM3D is most easily implemented on a Cartesian mesh, with some possibility of generalization to generalized curvilinear coordinates. Owing to the novelty and lim-

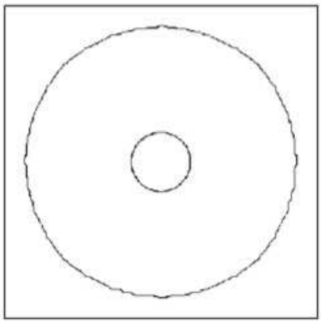

Fig. 10.10: Propagation of a circular flame front [3].

ited evaluation of LEM3D to date, further discussion of LEM-based subgrid closure focuses on the splicing strategy.

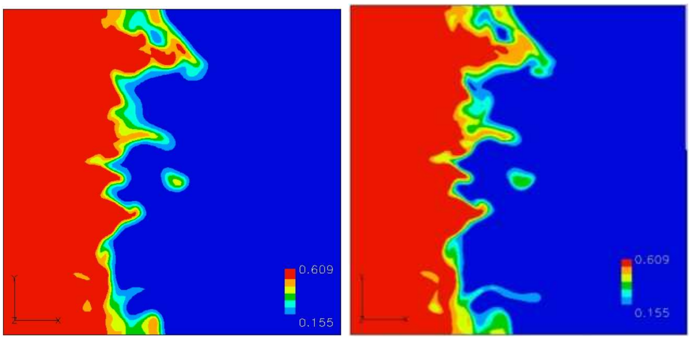

Fig. 10.11: DNS and LEMDNS of premixed flame-turbulence interaction. Reprinted from [63] with permission from Elsevier.

10.7 LEMLES Applications to Reacting Flows

As cited above, the LEMLES has been used quite extensively for a range of problems from simple canonical flame-turbulence interactions to complex flows in gas turbine combustors. In the following we touch upon some key results primarily to highlight the predictive ability of the LEMLES approach. An underlying theme in all these comparisons is that the basic LEMLES approach is identical for all cases. The only changes occurring are the changes in the LES geometry, test conditions

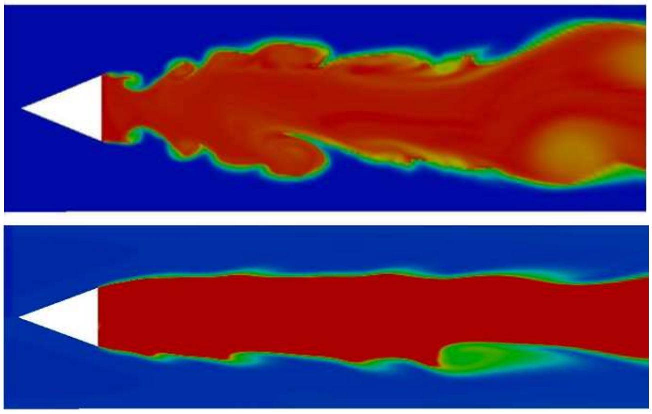

Fig. 10.12: Flame structure predicted behind a triangular bluff body. (a) LEMLES and (b) EBULES. Reprinted from [60].

and appropriate boundary conditions. In the following, we summarize some key results primarily to highlight the capability of the approach. Cited references have more detailed analysis and interpretations.

We begin with application to premixed combustion behind a triangular bluff body [60] that has been extensively studied in the past by various LES methods and closures. Here, we compare a simple subgrid EBU closure with the LEMLES to highlight some features. EBULES is a very simple closure for the reaction kinetics and therefore is used extensively in the literature. It strengths and limitations are well known and it is not the intent here to focus on these issues. Furthermore, other flame closure methods [15, 16] have also proven quite accurate for this test case and therefore, the current comparison is primarily to provide a reference. As shown in Fig. 10.12 and Fig. 10.13 show some key differences between the two predictive methods. The LEMLES flame structure is more wrinkled and its spreading is increased due to its increase burning rate. This is reflected in the mean temperature radial profile and the better agreement with the Reynolds stress measurements. Other premixed studies [4, 5, 10, 61, 63] have demonstrated that LEMLES has the ability to not only capture the flame propagation speed and structure, it also enables better prediction of the flame-turbulence interactions.

A more recent study focused on the ability of the LEMLES approach to capture complex flame structures in both premixed and non-premixed combustion in a special combustor. The Stagnation Point Reverse Flow (SPRF) is a low NOx combustor [77] that employs exhaust gas recirculation to achieve stable combustion in lean conditions while minimizing NOx and CO emissions. In this combustor, flame stabilization is achieved via a high-temperature downstream stagnation region. The schematic of the device shown in Fig. 10.14 consists of a generic can combustor with the inlet and the exhaust on the same end of the combustor. This design enables the EGR-preheated air to provide a high temperature and stable combustion

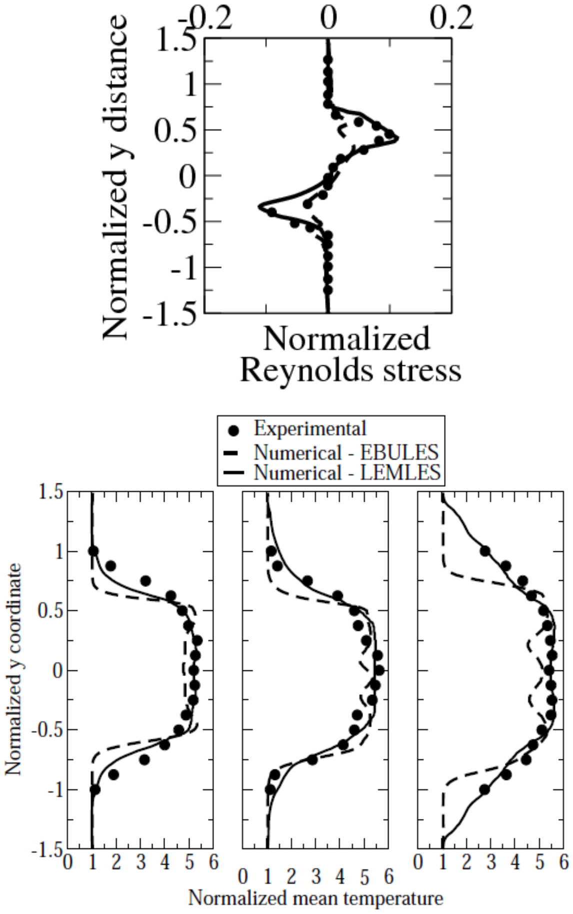

Fig. 10.13: The time-averaged radial profiles behind the bluff body. (a) Reynolds stress, and (b) mean temperature at three axial locations behind the bluff body. Reprinted from [60].

environment. Modeling the flow and flame structure in this device is complicated by the interaction between various features of flow confinement, stagnation, jet entrainment and product preheating and dilution through interaction of the incoming mixture with reverse co-flow. Experimentally, this combustor was shown to operate in both premixed and non-premixed combustion mode with low emissions but with very different flame structures, and therefore, it is a challenge for numerical prediction.

The recent study [77] simulated both premixed and non-prmeixed combustion using LEMLES and compared with other subgrid models such as the subgrid eddy break-up, artificially thickened flame and steady flamelets. Here, only representative

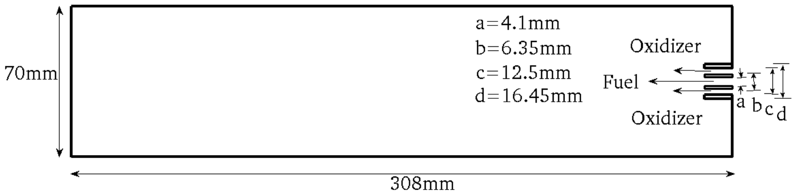

Fig. 10.14: Schematic and typical dimensions of the SPRF combustor.

results of the EBULES and LEMLES are discussed, although comparison with other models were reported earlier. Figure 10.15 compares the predictions with the averaged chemiluminescence field (note that although not clear here, the data does show that this flame is attached [21]). The EBULES flame structure is not clearly defined whereas the LEMLES predicts roughly the same flame length and reveals a flame anchored to the injector with heat release along the shear layer and in the downstream region of the combustor in agreement with the data. Comparison with data is reported elsewhere [77] and shows excellent agreement at nearly all locations.

When the combustor is operated in the non-premixed mode (with the fuel injected through the inner tube) the flame is lifted (Fig. 10.16). The LEMLES prediction is also a lifted flame whereas the EBULES did not capture this effect. The LEMLES flame structure and shape is somewhat different from the measurements but it is attributed to the reduced 1-step kinetics employed [77]. Regardless, the overall agreement with data is encouraging considering that the same model is employed for both premixed and non-premixed combustion without any ad hoc adjustments.

Finally, an application in spray combustion is discussed briefly although more details are given elsewhere [54, 57, 58]. The LDI combustor consists of a 60-degree, six helical swirl-vaned inlet that leads to a venturi, followed by a short divergent diffuser section that ends at the dump plane of a square combustion chamber. The swirler has outer diameter of 22.5 mm with the inner diameter of 8.8 mm. The calculated swirl number is 1.0 and Fig. 10.17(a) shows the schematic of the swirl generating blades in this combustor. The entire combustor (including the swirler assembly) is simulated with and without break-up modeling of the kerosene-air combustion system [57, 58]. Figure 10.17(b) shows the spray in the vicinity of the injector showing the breakup process. Details are in these cited references but here we focus on the nature of flame holding and the typical characteristics of the flame to highlight the ability of the LEMLES approach.

Centerline mean streamwise velocity is shown in Fig. 10.18(a). A prominent central re-circulation zone (CRZ) along the axis is observed for the non-reacting [57] (not shown) and reacting cases. This CRZ is created by the swirling inflow due to a radial pressure gradient caused by the centrifugal effect, which in turn gives rise to axial (and adverse) pressure gradient. For high swirl numbers, a strong coupling between axial and tangential velocity occurs and the adverse pressure gradient is strong enough to overcome the axial motion of fluid. This establishes a recircula-

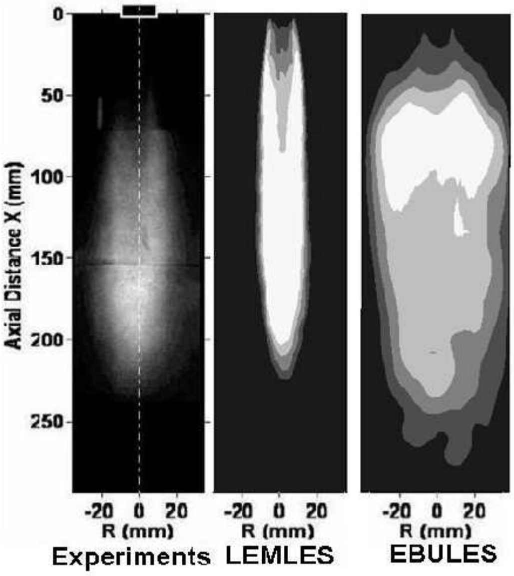

Fig. 10.15: Heat release in the premixed SPRF configuration. (a) Experiments, (b) LEMLES and (c) EBULES. Reprinted from [77] with permission from Elsevier.

tion zone, a form of vortex breakdown in the central region. This is the primary aerodynamic flame holding and stabilizing mechanism in gas turbine combustors.

Instantaneous flame structure is analyzed using the flame index, FI=$\nabla Y_F.\nabla Y_{O_2}$. To determine the flame regime, an indexed reaction rate is defined based on the flame index as: $\dot{\omega}_F^* = |\dot{\omega}_F|\frac{FI}{|FI|}$, and is shown in Fig. 10.18(b). Here, $\dot{\omega}_F$ is the fuel destruction rate. The stoichiometric equivalence ratio is shown as a thin line in the same figure. The flame is premixed when the FI (and consequently $\dot{\omega}_F^*$) is positive and diffusion when the FI is negative. In the central region, presence of fuel vapor in proximity of recirculating hot gases devoid of oxidizer generates a diffusion flame, as seen by light colored “V” shaped flame surface. This is confirmed by the coincidence between the flame and the stoichiometric line. Further outwards in the radial direction, significant dark colored contours are seen, indicating a premixed flame. Along the outer edges there is sufficient time for fuel-air mixing to complete before ignition, and thus, both non-premixed and premixed flames occur adjacently near the top half of the combustor with diffusion burning of fuel vapor evaporated from the particles that have gone through the primary flame without completely losing their identity. Since the LEMLES approach does not make any *a priori* assumptions regarding the nature of the flame it is able to capture the multi-faceted flame structure in these combustors.

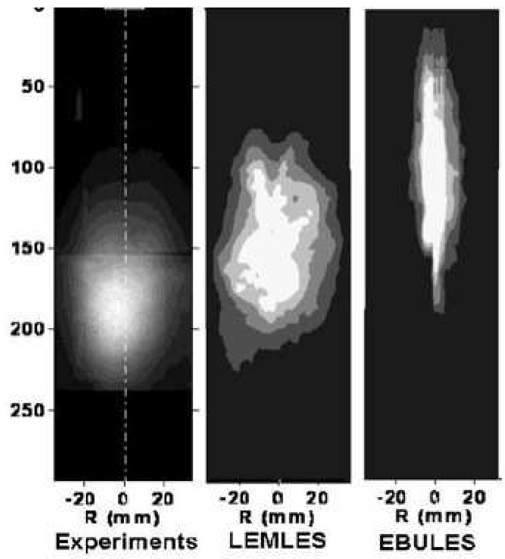

Fig. 10.16: Heat release in the non-premixed SPRF configuration.(a) Experiments, (b) LEMLES and (c) EBULES. Reprinted from [77] with permission from Elsevier.

10.8 Summary and Future Prospects

As summarized here the LEM has been used both as a stand-alone model and as a subgrid model for LES. Application of LEM as a RANS subgrid model has also been reported in some earlier and recent studies. The ability of this modeling strategy to study a wide range of reacting flows without any model adjustments (when combined with the LDKM closure for momentum there are no ad hoc adjustable parameters in the method) is one of the key strengths of this modeling approach. The robustness for a wide range of applications comes with an increase in cost. Efficient parallel implementation (the LEM subgrid model is highly parallel in its nature) can reduce the cost significantly but it is still expensive when compared to a steady flamelet or EBULES approach. On the other hand, the LEM-based closure can be used to go from one simulation regime to another without changing the model and this is a critical strength essential to study complex flame dynamics as in combustion instability, LBO and extinction-re-ignition processes. More recent successes in parametrizing the LEM in a neural network [68, 69, 71] offers a new potential for incorporating this model's ability in a cost effective LES strategy.

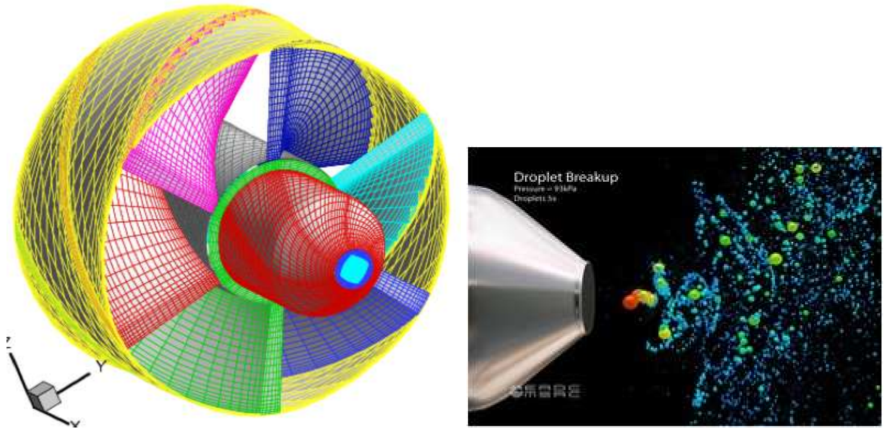

Fig. 10.17: The LDI swirler assembly and an instantaneous view of the droplets in the near -vicinity of the injector showing breakup. Reprinted from [58] with permission from Elsevier.

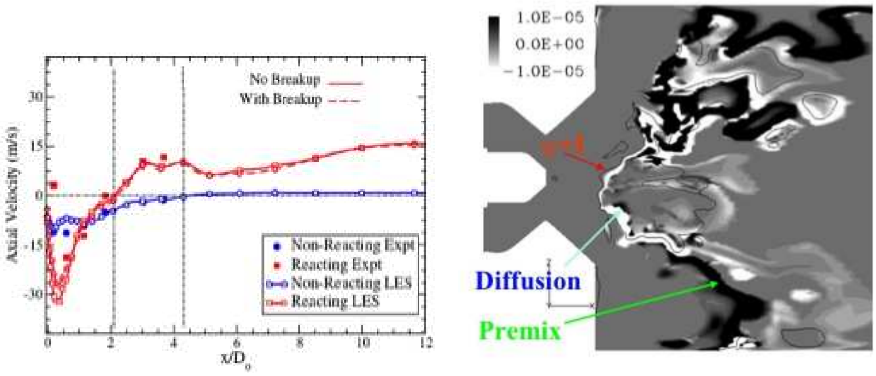

Fig. 10.18: Centerline velocity decay and flame structure in the LDI combustion. (a) Centerline axial velocity, (b) Flame index contours, with the black lines indicating the stoichiometric mixture fraction contour. Reprinted from [57] with permission from Elsevier.

Acknowledgement

The research at Georgia Tech is supported in part by Office of Naval Research, NASA Glenn Research Center, Air Force Office of Scientific Research, General Electric Aircraft Engine Company and Pratt & Whitney. This work in SNL is partially supported by the U.S. Department of Energy, Office of Basic Energy Sciences, Division of Chemical Sciences, Geosciences, and Energy Biosciences. Sandia National Laboratories is a multi-program laboratory operated by Sandia Corporation, a Lockheed Martin Company, for the United States Department of Energy under contract DE-AC04-94-AL85000.

References

1. Calhoon, W.H., Menon, S., Goldin, G.: Comparison of reduced and full chemical mechanisms for nonpremixed turbulent h2-air het flames. Combust. Sci. Technol. **104**, 115–141 (1995)
2. Chakravarthy, V., Menon, S.: Modeling of turbulent premixed flames in the flamelet regime. In: Proceedings of first International Symposium on Turbulent and Shear Flow Phenomena, pp. 189–194. Begel House (1999)
3. Chakravarthy, V., Menon, S.: Large-eddy simulations of turbulent premixed flames in the flamelet regime. Combust. Sci. Technol. **162**, 1–48 (2000)
4. Chakravarthy, V., Menon, S.: Large-eddy simulations of turbulent premixed flames in the flamelet regime. Combust. Sci. Technol. **162**, 175–222 (2000)
5. Chakravarthy, V., Menon, S.: Subgrid modeling of premixed flames in the flamelet regime. Flow Turbul. Combust. **65**, 23–45 (2000)
6. Chakravarthy, V., Menon, S.: Linear-eddy simulations of Reynolds and Schmidt number dependencies in turbulent scalar mixing. Phys. Fluids **13**, 488–499 (2001)
7. Cremer, M.A., McMurtry, P.A., Kerstein, A.R.: The effect of turbulence length-scale distribution on scalar mixing in homogeneous turbulent-flow. Phys. Fluids **6**, 2143–2153 (1994)
8. DesJardin, P.E., Frankel, S.H.: Assessment of turbulent combustion submodels using the Linear Eddy Model. Combust. Flame **104**, 343 (1996)
9. DesJardin, P.E., Frankel, S.H.: Linear-eddy modeling of nonequilibrium turbulent reacting flows with nonpremixed reactants. Combust. Flame **109**, 471–481 (1997)
10. Eggenspieler, G., Menon, S.: Combustion and emission modeling near lean blow-out in gas turbine engines. Prog. Comput. Fluid Dyn. **5**, 281–297 (2005)
11. El-Asrag, H., Menon: Large eddy simulation of a bluff-body stabilized swirling non-premixed flames. Proc. Combust. Inst. **31**, 1747–1754 (2007)
12. El-Asrag, H., Menon, S.: Simulation of soot formation in turbulent premixed flame. Combust. Flame **150**, 108–126 (2007)
13. El-Asrag, H., Menon, S.: Large eddy simulation of soot formation in a turbulent non-premixed jet flame. Combust. Flame **156**, 385–395 (2009)
14. Frankel, S.H., McMurtry, P.A., Givi, P.: Linear eddy modeling of reactant conversion and selectivity in turbulent flows. AIChE J. **41**, 259–270 (1995)
15. Fureby, C., Löfström, C.: Large-eddy simulations of bluff body stabilized flames. Proc. Combust. Inst. **25**, 1257–1264 (1994)
16. Fureby, C., Möller, S.I.: Large-eddy simulation of reacting flows applied to bluff body stabilized flames. AIAA J. **33**, 2339–2347 (1995)
17. Genin, F., Menon, S.: Studies of shock/turbulent shear layer interaction using large-eddy simulation. Computer Fluids **39**, 800–819 (2010)
18. Goldin, G.M., Calhoon, W.H., Menon, S.: A Linear eddy mixing model for steady non-premixed turbulent combustion. AIAA-1995-0379 (1995)
19. Goldin, G.M., Menon, S.: Scalar pdf construction model for turbulent non-premixed combustion. Combust. Sci. Technol. **125**, 47 – 72 (1997)
20. Goldin, G.M., Menon, S.: A comparison of scalar pdf turbulent combustion models. Combust. Flame **113**, 442 – 453 (1998)
21. Gopalakrishnan, P., Bobba, M.K., Seitzman, J.M.: Controlling mechnamisms for low nox emissions in a non-premixed stagnation point reverse flow combustor. Proc. Combust. Inst. **31**, 3401 – 3408 (2007)

22. Guilkey, J.E., Kerstein, A., McMurtry, P.A., Klewicki, J.C.: Effects of initial conditions on scalar statistics in pipe mixing. AIChE J. **43**, 1947–1954 (1997)
23. Guilkey, J.E., Kerstein, A.R., McMurtry, P.A., Klewicki, J.C.: Mixing mechanisms in turbulent pipe flow. Phys. Fluids **9**, 717–723 (1997)
24. Guilkey, J.E., Kerstein, A.R., McMurtry, P.A., Klewicki, J.C.: Long-tailed probability distributions in turbulent-pipe flow mixing. Phys. Rev. E **56**, 1753 – 1758 (1997)
25. Hawkes, E.R., Sankaran, R., Chen, J.H., Kaiser, S.A., Frank, J.H.: An analysis of lower-dimensional approximations to the scalar dissipation rate using direct numerical simulations of plane jet flames. Proc. Combust. Inst. **32**, 1455–1463 (2009)
26. Hawkes, E.R., Sankaran, R., Sutherland, J.C., Chen, J.H.: Scalar mixing in direct numerical simulations of temporally evolving plane jet flames with skeletal CO/H2 kinetics. Proc. Combust. Inst. **31**, 1633–1640 (2007)
27. Jaberi, F.A., Miller, R.S., Madnia, C.K., Givi, P.: Non-gaussian scalar statistics in homogeneous turbulence. J. Fluid Mech. **313**, 241–282 (1996)
28. Kalda, J., Morozenko, A.: Turbulent mixing: the roots of intermittency. New J. Phys. **10**, 093003 (2008)
29. Kerstein, A.R.: Linear-eddy model of turbulent scalar transport and mixing. Combust. Sci. Technol. **60**, 391–421 (1988)
30. Kerstein, A.R.: Linear-eddy model of turbulent transport II: Application to shear layer mixing. Combust. Flame **75**, 397–413 (1989)
31. Kerstein, A.R.: Linear-eddy model of turbulent transport. Part 3. Mixing and differential molecular diffusion in round jets. J. Fluid Mech. **216**, 411–435 (1990)
32. Kerstein, A.R.: Linear-eddy modeling of turbulent transport. Part V: Geometry of scalar interfaces. Phys. Fluids A **3**, 1110–1114 (1990)
33. Kerstein, A.R.: Linear-eddy modeling of turbulent transport. Part 6. Microstructure of diffusive scalar mixing fields. J. Fluid Mech. **231**, 361–394 (1991)
34. Kerstein, A.R.: Linear-eddy modeling of turbulent transport. 7. Finite-rate chemistry and multi-stream mixing. J. Fluid Mech. **240**, 289–313 (1992)
35. Kerstein, A.R.: Prandtl-number dependence of turbulent flame propagation. Phys. Rev. E **64**, 066306 (2001)
36. Kerstein, A.R., Cremer, M.A., McMurtry, P.A.: Scaling properties of differential molecular diffusion effects in turbulence. Phys. Fluids **7**(8), 1999–2007 (1995)
37. Kerstein, A.R., Krueger, S.K.: Linear eddy simulations of mixing in a homogeneous turbulent-flow. Phys. Rev. E **73**, 025302 (2006)
38. Kerstein, A.R., McMurtry, P.A.: Low wave-number statistics of randomly advected passive scalars. Phys. Rev. E **50**, 2057 (1994)
39. Kim, W.W., Menon, S.: A new incompressible solver for large-eddy simulations. Int. J. Num. Fluid Mech. **31**, 983–1017 (1999)
40. Kim, W.W., Menon, S.: Numerical simulations of turbulent premixed flames in the thin-reaction-zones regime. Combust. Sci. Technol. **160**, 119–150 (2000)
41. Kim, W.W., Menon, S., Mongia, H.C.: Large-eddy simulation of a gas turbine combustor flow. Combust. Sci. Technol. **143**, 25–62 (1999)
42. Krueger, S.K.: Linear eddy modeling of entrainment and mixing in stratus clouds. J. Atmos. Sci. **50**, 3078–3090 (1993)
43. Krueger, S.K., Su, C.W., McMurtry, P.A.: Modeling entrainment and finescale mixing in cumulus clouds. J. Atmos. Sci. **54**, 2697 – 2712 (1997)
44. McMurtry, P.A., Gansauge, T.C., Kerstein, A.R., Krueger, S.K.: Linear eddy simulations of mixing in a homogeneous turbulent-flow. Phys. Fluids A **5**, 1023 – 1034 (1993)
45. McMurtry, P.A., Menon, S., Kerstein, A.R.: A new subgrid model for turbulent combustion: Application to hydrogen-air combustion. Proc. Combust. Inst. **24**, 271–278 (1993)
46. Menon, S.: Computational and modeling constraints for large-eddy simulations of turbulent combustion. Int. J. Engine Res. **1**, 209–227 (2000)
47. Menon, S., Calhoon, W.H.: Subgrid mixing and molecular transport modeling for large-eddy simulations of turbulent reacting flows. Proc. Combust. Inst. **26**, 59–66 (1996)

48. Menon, S., Calhoon, W.H., Goldin, J.R., Kerstein, A.R.: Effects of molecular transport on turbulent-chemistry interactions in hydrogen-argon-air jet diffusion flame. Proc. Combust. Inst. **25**, 1125–1131 (1994)
49. Menon, S., Kerstein, A.R.: Stochastic simulation of the structure and propagation rate of turbulent premixed flames. Proc. Combust. Inst. **24**, 443–450 (1992)
50. Menon, S., Kim, W.W.: High Reynolds number flow simulations using the localized dynamic subgrid-scale model. AIAA-96-0425 (1996)
51. Menon, S., McMurtry, P., Kerstein, A.R.: A linear eddy mixing model for large eddy simulation of turbulent combustion. In: B. Galperin, S. Orszag (eds.) LES of Complex Engineering and Geophysical Flows, pp. 287–314. Cambridge University Press, Cambridge, UK (1993)
52. Menon, S., McMurtry, P.A., Kerstein, A.R., Chen, J.Y.: A new mixing to predict Nox production in turbulent hydrogen-air jet flame. J. Prop. Power **10**, 161–168 (1994)
53. Menon, S., Pannala, S.: Subgrid combustion simulations of reacting two-phase shear layers. AIAA-98-3318 (1998)
54. Menon, S., Patel, N.: Subgrid modeling for LES of spray combustion in large-scale combustors. AIAA J. **44**, 709–723 (2006)
55. Menon, S., Yeung, P.K., Kim, W.W.: Effect of subgrid models on the computed interscale energy transfer in isotropic turbulence. Computers Fluids **25**, 165–180 (1996)
56. Oevermann, M., Schmidt, H., Kerstein, A.R.: Investigation of autoignition under thermal stratification using linear eddy modeling. Combust. Flame **155**, 370 (2008)
57. Patel, N., Kirtas, M., Sankaran, V., Menon, S.: Simulation of spray combustion in a lean direct injection combustor. Proc. Combust. Inst. **31**, 2327–2334 (2007)
58. Patel, N., Menon, S.: Simulation of spray-turbulence-flame interactions in a lean direct injection combustor. Combust. Flame **153**, 228–257 (2008)
59. Pope, S.B.: Pdf methods for turbulent reactive flows. Prog. Energy Combust. Sci. **11**, 119–192 (1985)
60. Porumbel, I., Menon, S.: Large-eddy simulation of bluff body stabilized premixed flames. AIAA-2006-0152 (2006)
61. Sankaran, V., Menon, S.: Structure of premixed flame in the thin-reaction-zones regime. Proc. Combust. Inst. **28**, 203–210 (2000)
62. Sankaran, V., Menon, S.: LES of scalar mixing in supersonic shear layers. Proc. Combust. Inst. **30**, 2835–2842 (2005)
63. Sankaran, V., Menon, S.: Subgrid combustion modeling of 3-d premixed flames in the thin-reaction-zone regime. Proc. Combust. Inst. **30**, 575–582 (2005)
64. Sankaran, V., Porumbel, I., Menon, S.: Large-eddy simulation of a single-cup gas turbine combustor. AIAA-2003-5083 (2003)
65. Sannan, S., Weydahl, T., Kerstein, A.R.: to appear (2010)
66. Schenck, H.W., Wendt, J.O.L., Kerstein, A.R.: Mixing characterization of transient puffs in a rotary kiln incinerator. Combust. Sci. Technol. **116**, 427 –453 (1996)
67. Schmidt, R.C., Kerstein, A.R., McDermott, R.: ODTLES: A multi-scale model for 3D turbulent flow based on one-dimensional turbulence modeling. Comput. Meth. Appl. Mech. Engg **199** 865–880 (2009)
68. Sen, B.A., Hawkes, E., Menon, S.: Large eddy simulation of extinction and reignition with artificial neural networks based chemical kinetics. Combust. Flame **157**, 566–578 (2010)
69. Sen, B.A., Menon, S.: Artificial neural networks based chemistry-mixing subgrid model for LES. AIAA-2009-0241 (2009)
70. Sen, B.A., Menon, S.: Turbulent premixed flame modeling using artificial neural network based chemical kinetics. Proc. Combust. Inst. **32**, 1605–1611 (2009)
71. Sen, B.A., Menon, S.: Linear eddy mixing and artificial neural networks for LES sub-grid chemistry closure. Combust. Flame **157**, 62–74 (2010)
72. Smith, T., Menon, S.: One-dimensional simulations of freely propagating turbulent premixed flames. Combust. Sci. Technol. **128**, 99–130 (1996)
73. Smith, T.M., Menon, S.: Model simulations of freely propagating turbulent premixed flames. Proc. Combust. Inst. **26**, 299–306 (1996)

74. Smith, T.M., Menon, S.: Large-eddy simulations of turbulent reacting stagnation point flows. AIAA-97-0372 (1997)
75. Smith, T.M., Menon, S.: Subgrid combustion modeling for premixed turbulent reacting flows. AIAA-98-0242 (1998)
76. Su, C.W., Krueger, S.K., McMurtry, P.A., Austin, P.H.: Linear eddy modeling of droplet spectral evolution during entrainment and mixing in cumulus clouds. Atmos. Res. **47**, 41 – 58 (1998)
77. Undapalli, S., Menon, S.: LES of premixed and non-premixed combustion in a stagnation point reverse flow combustor. Proc. Combust. Inst. **32**, 1537–1544 (2009)
78. Woosley, S.E., Kerstein, A.R., Sankaran, V., Aspden, A.J., Roepke, F.K.: Type Ia supernovae:Ccalculations of turbulent flames using the linear eddy model. Astrophys. J. **704**, 255 – 273 (2009)
79. Wu, J., Menon, S.: Aerosol dynamics in the near-field engine exhaust plumes. J. Appl. Meteo. **40**, 795–809 (2001)
80. Zimberg, M.J., Frankel, S.H., Gore, J.P., Sivathanu, Y.R.: A study of coupled turbulent mixing, soot chemistry, and radiation effects using the linear eddy model. Combust. Flame **113**, 454 – 469 (1998)